Research Article

Siqi He, Tongjiang Peng*, Hongjuan Sun, Dongshan Luo, Qing Xiao, Qian Geng

Kinetics of Iron Removal From Ti-Extraction Blast Furnace Slag by Chlorination Calcination

https://doi.org/10.1515/chem-2019-0124
received June 1, 2019; accepted August 29, 2019.

Abstract: In this research, ammonium chloride was used to calcine Ti-extraction blast furnace slag (EBFS) with the aim of removing iron from it. The influences of calcination temperature, ammonium chloride to EBFS mass ratio and particle size on the rates of iron removal were investigated. The results show that the rate of iron removal increased to almost 100% with increases in calcination temperature and the NH_4Cl to EBFS mass ratio, but decreased with increases in particle size. Iron is removed in the form of ferric chloride gas, and ammonium chloride can be recycled by recrystallization after decomposition. The bagdasarrym model was used to describe the calcination process at temperatures below 261°C, which was controlled by nonisothermal crystallization. The reaction kinetic equation was obtained and the apparent activation energy of 67.21 kJ/mol. Ferric chloride reaction product existed in the calcined slag in an amorphous solid state. The shrinking core model was used to describe the calcination process at temperatures above 261°C, which was controlled by surface chemical reactions. The reaction kinetic equation was obtained and the apparent activation energy was found to be 42.05 kJ/mol.

Keywords: Ti-extraction blast furnace slag; iron removal; chlorination calcination; kinetics

***Corresponding author: Tongjiang Peng,** Key Laboratory of Ministry of Education for Solid Waste Treatment and Resource Recycle, Southwest University of Science and Technology, Mianyang 621010 Sichuan, China; Institute of Mineral Materials & Application, Southwest University of Science and Technology, Mianyang 621010, Sichuan, China, E-mail: tjpeng@swust.edu.cn
Siqi He, Hongjuan Sun, Dongshan Luo, Qing Xiao, Qian Geng, Key Laboratory of Ministry of Education for Solid Waste Treatment and Resource Recycle, Southwest University of Science and Technology, Mianyang 621010 Sichuan, China; Institute of Mineral Materials & Application, Southwest University of Science and Technology, Mianyang 621010, Sichuan, China

1 Introduction

In Panzhihua, China, over 60 million tons of Ti-bearing blast furnace slag (TBFS) is produced. It causes severe environmental problems such as groundwater contamination via the leaching of hazardous heavy metals, while particulates are emitted into the surrounding air [1]. At present, high-temperature carbonization-low-temperature chlorination is the main process used to utilise TBFS [2]. This process has a high titanium extraction rate; however, it produces a chlorine-containing waste residue called Ti-extraction blast furnace slag (EBFS), which is difficult to treat and can cause serious environmental pollution.

After chlorine removal, EBFS is mainly used to produce low-value-added products such as cement mortar admixtures [3] and bricks [4-5]. Based on its complex composition and amorphous phase structure, our research group used EBFS to produce glass-ceramics with good properties [6-7]. The chloride component escapes from EBFS during a calcination process; however, deleterious impurities can remain, usually in the form of iron compounds, which can discolour glass-ceramic products. This limits the commercial applications of glass-ceramics. Therefore, it is necessary to remove iron from EBFS before using it in glass-ceramics. Iron can be removed by two methods including: 1) a physical separation process that aims to remove iron-containing minerals, and 2) chemical treatment that dissolves iron compounds bonded at the surface or existing as mineral grains [8]. The appropriate method for the removal of iron from an industrial solid waste depends on its mineralogical form and iron distribution.

Based on a mineralogical study of EBFS, this work aims to investigate the iron removal from EBFS by ammonium chloride calcination. The iron component in EBFS reacts with ammonium chloride to form ferric chloride, which escapes from the slag in a gaseous state at a certain temperature. The process conditions, such as calcination temperature, mass ratio of NH_4Cl to EBFS and particle size, were assessed. Furthermore, the

chlorination calcination kinetics of iron was studied, which can provide a theoretical guide for future process optimization and industrial applications.

2 Materials And Methods

2.1 Mineralogical analysis of EBFS

Samples of EBFS were collected from Panzhihua Iron and Steel Co. Ltd., Sichuan, China. X-ray Fluorescence (XRF) was used to analyse the chemical components of EBFS, X-ray Diffraction (XRD) was used for mineral phase analysis, X-ray Photoelectron Spectroscopy (XPS) was used for valence analysis of the iron in EBFS, Scanning Electron Microscope-Energy Dispersive Spectroscopy (SEM-EDS) was used to analyse the morphology and iron distribution of EBFS, and Thermogravimetric Analysis-Differential Scanning Calorimetry (TG-DSC) was used for thermal stability analysis.

2.2 Process of calcination with ammonium chloride

Calcination was carried out in a furnace with programmed temperature control. Firstly, a certain amount of ammonium chloride was put into a 10 g EBFS sample and stirred in a 100 mL ceramic crucible, which was then placed in the furnace. The experiments were repeated under various experimental conditions. The process design is represented in Table 1. After being calcined, The calcined product obtained below 260°C was leached in water to obtain the leached product. The leached product and the calcined product obtained above 261°C was characterized by XRF. The % iron removal (R) was calculated according to Equation (1):

$$R = \frac{m_2}{m_1} \times 100\% \quad (1)$$

where m_1 and m_2 are the masses of Fe_2O_3 in the EBFS and calcined product or leached product, respectively.

Ethical approval: The conducted research is not related to either human or animal use.

Table 1: Design of the experiment.

Parameters	Levels
Time (min)	0, 5, 10, 15, 20, 25, 30, 35, 40, 50, 60
Temperature (°C)	180, 220, 260, 290, 310, 335, 350
Mass ratio of NH_4Cl to EBFS	1.0, 1.5, 2.0, 2.5
Average particle size (μm)	300, 200, 100, 74

Table 2: Chemical composition of EBFS samples (%).

CaO	SiO_2	Al_2O_3	TiO_2	MgO	Fe_2O_3	Cl	SO_3
32.45	27.72	13.37	8.68	7.62	4.39	2.96	0.84
MnO	K_2O	Na_2O	BaO	SrO	P_2O_5	ZrO_2	Y_2O_3
0.81	0.67	0.26	0.1	0.06	0.04	0.03	0.01

3 Results And Discussion

3.1 Characterization of EBFS samples

The loss on ignition (LOI) of EBFS was 12.92%. On the basis of the XRF results, it contained 4.39% Fe_2O_3 (Table 2). XRD of the EBFS (Figure 1) shows that the main diffraction peaks are d_{111}=2.49 Å, d_{200}=2.16 Å, d_{220}=1.52 Å and d_{311}=1.30 Å, which are characteristic peaks of its titanium carbide (TiC) (reference code: 00-032-1383) [9]. Besides, there are some amorphous substances in EBFS, the chemical bond in amorphous compounds is easier to break and synthesize than that in the crystal of the same substance. So the EBFS sample had high reactivity [10]. XPS was used to characterize the Fe oxidation state (Figure 2). The supported Fe_2O_3 was characterized by a spin-coupled doublet for curve fitting of $Fe2p_{3/2}$ and $Fe2p_{1/2}$ at 712.2 eV and 725.6 eV, respectively [11-12]. The supported FeO was characterized by a spin-coupled doublet for curve fitting of $Fe2p_{3/2}$ and $Fe2p_{1/2}$ at 711 eV and 723.7 eV, respectively, which indicates that both Fe^{2+} and Fe^{3+} species were present in the EBFS [13]. Figure 3 shows the SEM-EDS determined distribution of iron in the EBFS samples. The EBFS particles had no specific morphology and could be divided into two types: those with smooth and dense surfaces, and those with rough and loose surfaces. Surface scanning analysis indicates that the distribution of iron was very dispersed. Hence, it would be difficult to remove iron by beneficiation and a chemical method would be better.

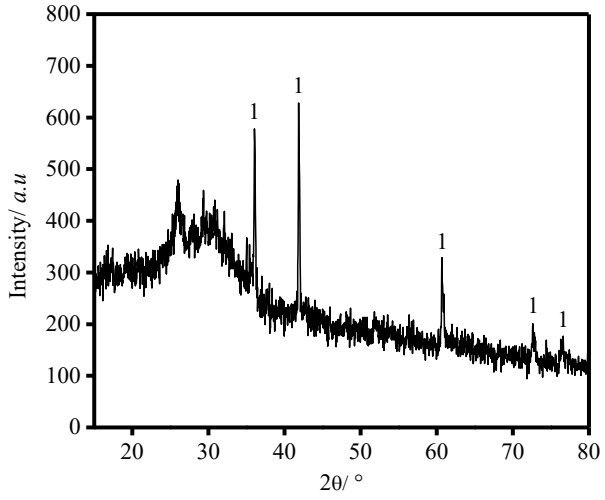

Figure 1: XRD pattern of EBFS samples. 1=titanium carbide.

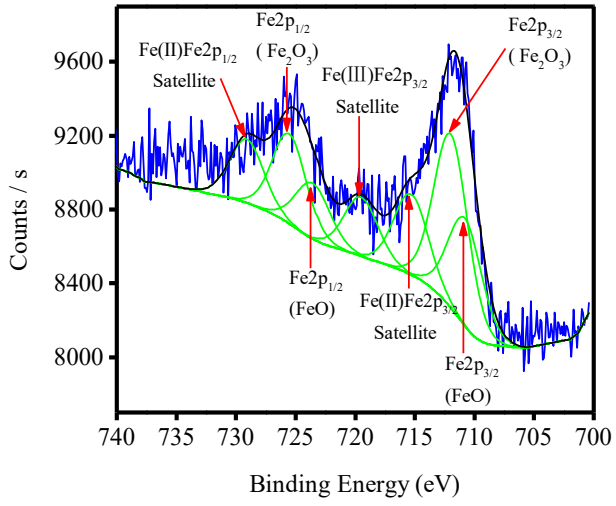

Figure 2: XPS spectra in the Fe2p region of EBFS.

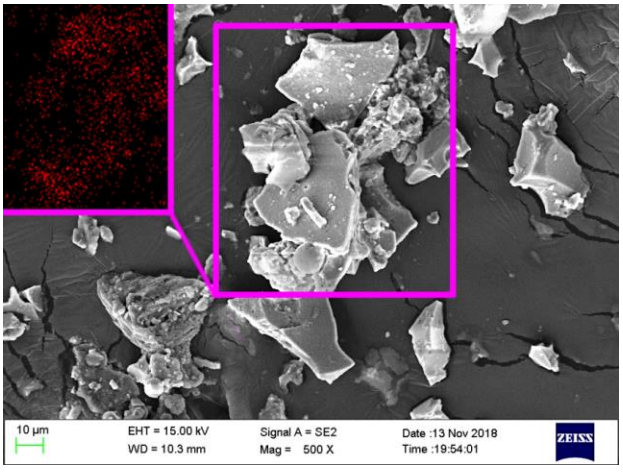

Figure 3: SEM-EDS images of EBFS.

3.2 Effect of experimental conditions on iron removal

3.2.1 Effect of calcination temperature

The mixture of NH_4Cl and EBFS was calcined at 180, 220, 260, 290, 310, 335 and 350°C for 1 h, with the mass ratio of NH_4Cl to EBFS and the particle size of EBFS held at 1.8:1 and 250 μm, respectively. The results shown in Figure 4 revealed that temperature had a strong influence on the iron removal rate, which was > 60% at temperatures > 335°C. Figure 5 shows the TG-DSC diagram for the mixture of NH_4Cl and EBFS, which has four endothermic peaks and two mass-loss regions from 170–350°C. The DSC curve of the mixture shows two small endothermic peaks at 172.1°C and 210.9°C due to the reaction of solid ammonium chloride with iron components in the EBFS. The DSC curve also shows a sharp endothermic peak at 261.1°C due to ammonium chloride being decomposed into ammonia and hydrogen chloride, resulting in a mass loss of 17.2% [14]. The DSC curve shows a small endothermic peak at 310.2°C due to the reaction of gaseous hydrogen chloride with iron components in the EBFS that formed ferric chloride gas, resulting in a mass loss of 5.2%. The reaction temperature is slightly lower than the thermodynamic calculation temperature of the reaction between Fe_2O_3 and HCl. It may be that other components in EBFS play a catalytic role in the reaction [15]. Therefore, an increase in the removal rate with increases in temperature could be attributed to a change of the state of the calcination additives leading to an increase in the reaction area between EBFS and the calcination additives.

3.2.2 Effect of the NH_4Cl to EBFS ratio

The effect of increasing the mass ratio of NH_4Cl to EBFS on iron removal is shown in Figure 6, with the calcination temperature and average particle size held at 335°C and 250 μm, respectively. An increase in the NH_4Cl to EBFS mass ratio was observed to have some influence on the iron removal rate. At low ratios, the NH_4Cl decomposed less hydrogen chloride gas, resulting in a low overall concentration of hydrogen chloride in the reaction system. Meanwhile, an increase in the ratio contributed to an increased concentration of hydrogen chloride gas in the reaction system, thus increasing the reaction rate of calcination additives and iron-containing particles in the EBFS.

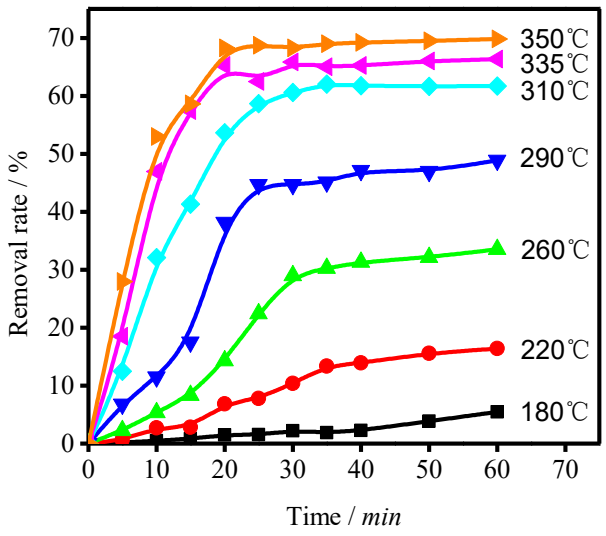

Figure 4: Effect of temperature on iron removal rates with time.

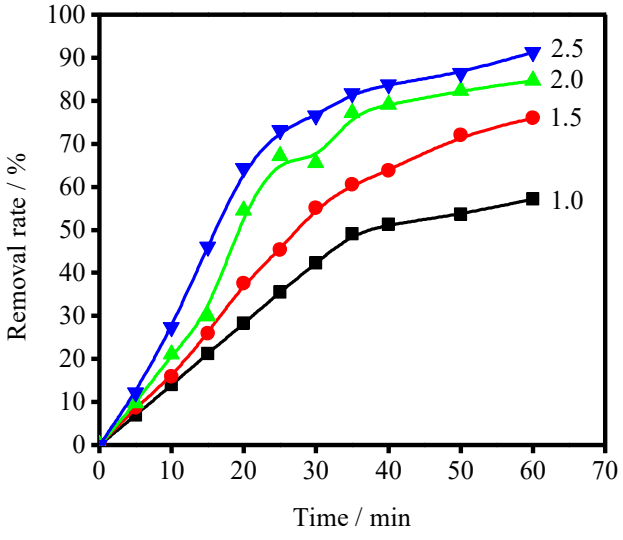

Figure 6: Effect of various NH_4Cl to EBFS mass ratios on iron removal rate over time.

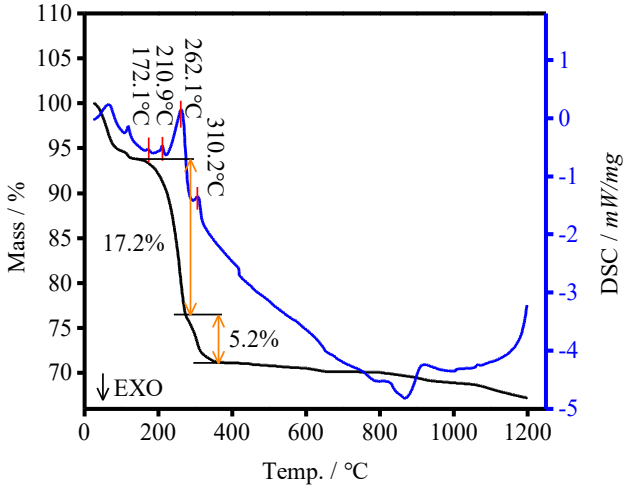

Figure 5: TG-DSC analysis of the NH_4Cl and EBFS mixture.

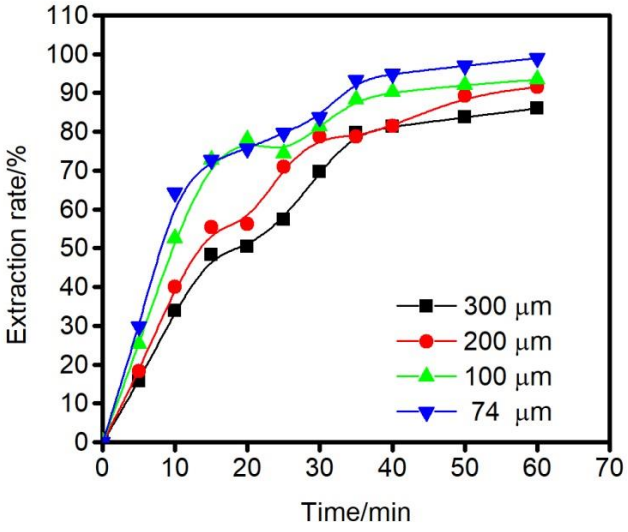

Figure 7: Effect of various particle sizes on iron removal rate over time.

3.2.3 Effect of particle size

The influence of average particle size fractions on the removal rate of iron is shown in Figure 7, with the reaction temperature and mass ratio of NH_4Cl to EBFS held at 335°C and 2.0:1. The results indicate that iron removal rates increased with decreases in the EBFS particle size. A decrease in particle size would contribute to an increase in the specific surface area, leading to much-improved heat and mass transfer rates and facilitating faster liberation of the iron component [16].

3.3 Phase analysis of calcined products and condensated products

As seen in the XRD patterns of the calcined product at 220, 260, 335 and 350°C with the mass ratio of NH_4Cl to EBFS and the particle size held at 1.8:1 and 250 μm in Figure 8, comparing with XRD of EBFS (Figure 1), the number and the intensity of the diffraction peaks of titanium carbide (TiC) decreased until they disappeared after calcination. The diffraction peaks of ammonium chloride appeared in the calcined products at 220 and 260°C. However, there is no diffraction peaks of ammonium chloride in the calcined products at 335 and 350°C. This is consistent with the

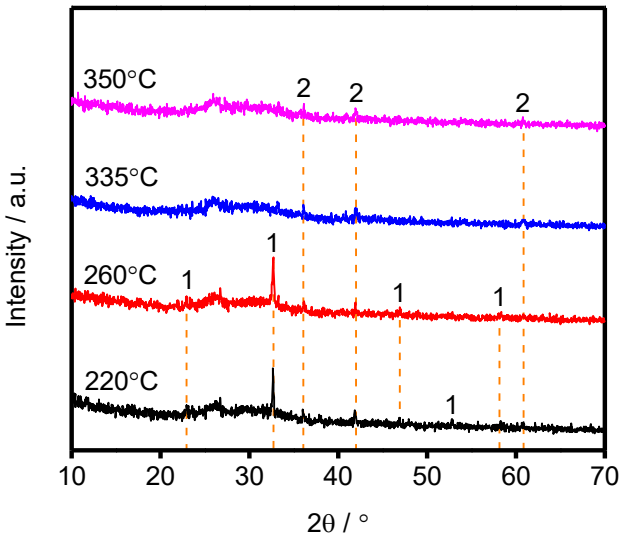

Figure 8: XRD patterns of the calcined product obtained at different temperatures: 1-Ammonium Chloride, 2- Titanium Carbide.

TG-DSC result (Figure 5) that ammonium chloride being decomposed into ammonia and hydrogen chloride when the temperature is higher than 261°C. This phenomenon shows that ammonium chloride will not remain in the calcined product when the calcination temperature is higher than 261°C, which is beneficial to the application of EBFS after iron removal. There are no diffraction peaks of ferric chloride in calcined product. The reason is that ferric chloride is gaseous when the calcination temperature is higher than 310.2°C, and ferric chloride may exist in amorphous state when the temperature is less than 310.2°C.

Gas produced by calcination of EBFS at 335°C, and the products of gas condensation show three distinct color ranges on the wall of quartz tube (Figure 9). The XRD pattern of the condensated products in three color ranges shown in Figure 9A, B, C revealed that white condensated product was calcination additive ammonium

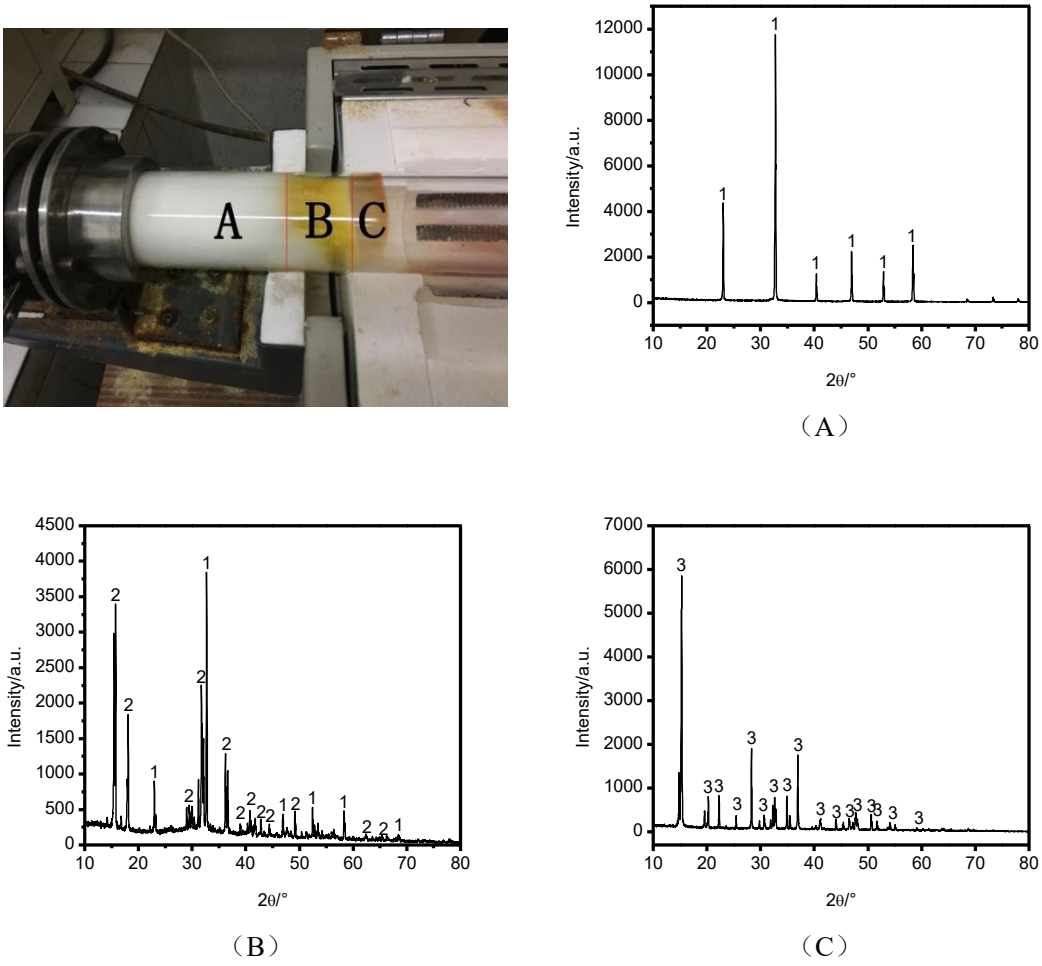

Figure 9: XRD patterns of condensation products of volatile gases calcined at 335 ºC: 1- Ammonium Chloride (NH_4Cl), 2- Ammonium Aqua Iron Chloride($(NH_4)_2FeCl_5H_2O$), 3- Iron Chloride Hydrate ($FeCl_3{\cdot}6H_2O$).

chloride which is formed by hydrogen chloride gas and ammonia gas decomposed from ammonium chloride, yellow condensated product was the mixture of ammonium chloride and ammonium aqua iron chloride, brown condensated product was iron chloride hydrate. This phenomenon shows that iron can be successfully removed by calcination with ammonium chloride. Iron exists in the form of ferric chloride and can be recovered by condensation, the calcination additives ammonium chloride can also be recycled by recrystallization after decomposition.

3.4 Calcination kinetics analysis

3.4.1 Temperatures less than 261°C

Ammonium chloride is solid at calcination temperatures lower than 261°C, so the chlorination reaction is a solid-solid reaction that forms a solid phase. The typical rate-controlling step of solid-solid reaction are the interfacial chemical reaction, diffusion control and nonisothermal crystallization process. The step with the highest kinetic resistance is the rate controlling step [17-18]. Table 3 shows the integrated rate equations. Experimental data obtained at 180, 220 and 260°C were compared with the three models, with the results shown in Figure 10 [19-21]. It can be seen that the plots of ln[-ln(1-r_{Fe})] had a very good linear relationship with lnt, with a fitting degree higher than 0.9. This indicates that the calcination rate was controlled by regional nucleation reactions, the most appropriate reaction model is the bagdasarrym model [19]. The reaction rate constant ln*k* and its model equation at different temperatures are presented in Table 4. According to the kinetic equation, we can know that when n ≈ 1, the number of growth directions of the product nucleus is α = 0. So, it can be judged that the chlorination calcination reaction is completed in one step and the chlorination product is amorphous at temperatures < 261°C [22]. This is consistent with the conclusions of the experiment—that ferric chloride in the calcined product obtained at < 261°C is in an amorphous phase. The relationship between reaction rate and temperature is well established and can be modelled with the Arrhenius equation, as expressed below.

$$k_r = A\mathrm{e}^{-E\mathrm{a}/RT} \tag{2}$$

$$\ln k_r = -\frac{E_a}{RT} + \ln A \tag{3}$$

Table 3: Integrated rate equations for the solid-solid reaction.

Rate-controlling step	Rate equation
Interfacial chemical reaction	$(1\text{-}rFe)^{-2/3}\text{-}1=kr1t$
Diffusion control	$1\text{-}2rFe/3\text{-}(1\text{-}rFe)^{2/3}=kr2t$
Nonisothermal crystallization	$\ln[-\ln(1\text{-}rFe)]=\ln kr3+n\ln t$

rFe- iron removal degree; *t*- time (min); *kr*- apparent rate constant (min^{-1}); *n*- $n=\delta+\alpha$, δ is the number of steps in series reaction and α is the number of growth directions of product nuclei.

Table 4: Parameters of ln[-ln(1-r_{Fe})] vs ln*t* obtained at temperatures of 160°C, 200°C and 230°C.

Temperature (°C)	Apparent rate constant ln*k*	Fitting equation
180	-8.40582	ln[-ln(1-*rFe*)]= -8.40582+1.31927ln*t*
220	-7.02595	ln[-ln(1-*rFe*)]= -7.02595+1.37603ln*t*
260	-5.72542	ln[-ln(1-*rFe*)]= -5.72542+1.27014ln*t*

where *kr* is the rate constant, *A* is the frequency factor, E_a is the apparent activation energy (J/mol), *R* is the mole gas constant (*R* = 8.314 J/mol) and *T* is the thermodynamic temperature.

The corresponding relationship between ln*kr* and 1/*T* is shown in Figure 11. The apparent activation energy of iron removal is estimated to be 67.21 kJ/mol according to the slopes of the straight lines in Figure 11, with *A* estimated as is 12.23×10^3 according to the intercept. Therefore, the semi-empirical kinetic equation is

$$\ln[-\ln(1-r_{Fe})] = ln12.23 \times 10^3 e^{-\frac{67210}{RT}} + lnt$$

where r_{Fe} is the fraction of Fe removed, *R* is the molar gas constant (*R* = 8.314 J/mol), *T* is the calcination temperature (K), *t* is the reaction time (min).

Because the ferric chloride calcined product is in an amorphous solid state at calcination temperatures below 261°C, solid ferric chloride cannot escape from the reaction system to achieve the purpose of iron removal. Hence, the dynamics of different NH_4Cl:EBFS mass ratios and EBFS particle sizes at calcination temperatures below 261°C are not discussed.

3.4.2 Temperatures above 261°C

Ammonium chloride decomposes into ammonia gas and hydrogen chloride gas at calcination temperatures higher than 261°C. The reaction product, ferric chloride, is a gas at this temperature, so the reaction between hydrogen chloride and the iron component of EBFS is a solid-gas

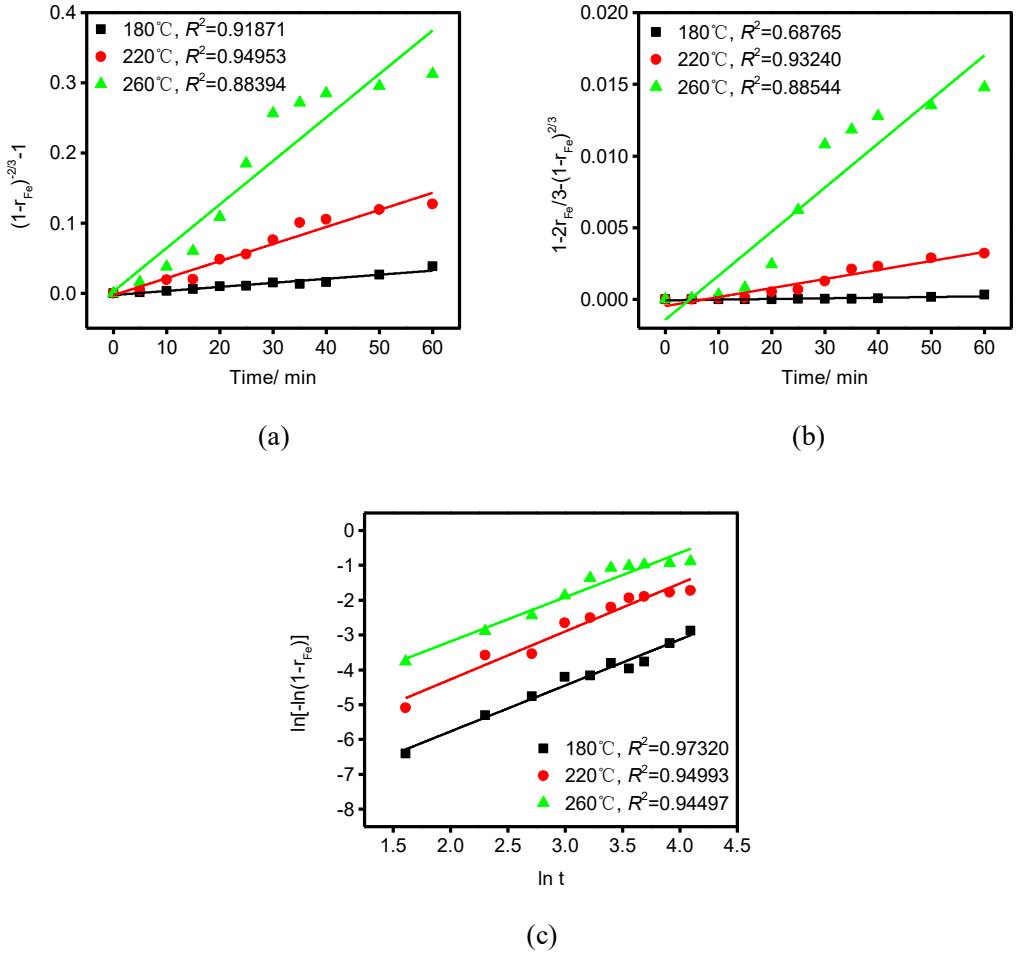

Figure 10: Comparison between plots of (a) $(1 - r_{Fe})^{-2/3} - 1$ and (b) $1 - 2r_{Fe}/3 - (1 - r_{Fe})^{2/3}$ vs time, (c) $\ln[-\ln(1 - r_{Fe})]$ vs $\ln t$.

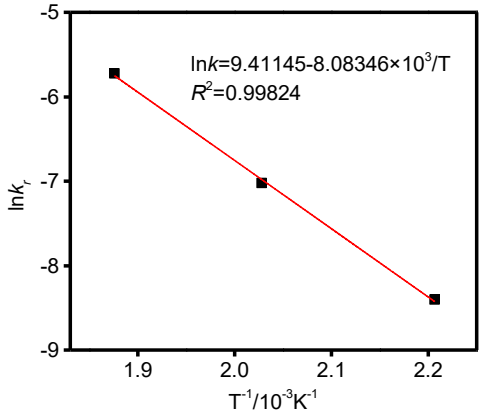

Figure 11: Arrhenius plot between lnkr and $1/T$ for the calculation of activation energy. The values of K_r were calculated by using the bagdasarrym model.

reaction. Because EBFS particles have dense surfaces, which can be considered as non-porous particles, and the iron-containing particles gradually shrink during calcination, so the most appropriate reaction model is the shrinking core model [23-25]. In the chlorination calcination system, the ferric chloride gas is formed by chlorination of iron-containing minerals. Because the iron-containing minerals are widely distributed and the total iron content in EBFS is relatively low, the release of ferric chloride gas does not have a significant impact on the morphology of the EBFS particles. This results in the calcination process being controlled by diffusion through the EBFS particle layer or chemical reactions at the surfaces of the EBFS particles [17]. Integrated rate equations for the shrinking core model are shown in Table 5 [20].

The linear regression analysis of experimental data obtained at temperatures of 290, 310, 335 and 350°C using the equations in Table 5. Figure 12 compares the plots of $1 - 2(1 - r_{Fe}) - 3(1 - r_{Fe})^{2/3}$ and $1 - (1 - r_{Fe})^{1/3}$ versus time at calcination temperatures of 290, 310, 335 and 350°C with a NH_4Cl to EBFS mass ratio of 1.8:1 and average particle size of 250 μm. The results show that there are very good linear relationships in the plots of $1 - (1 - r_{Fe})^{1/3}$ vs time.

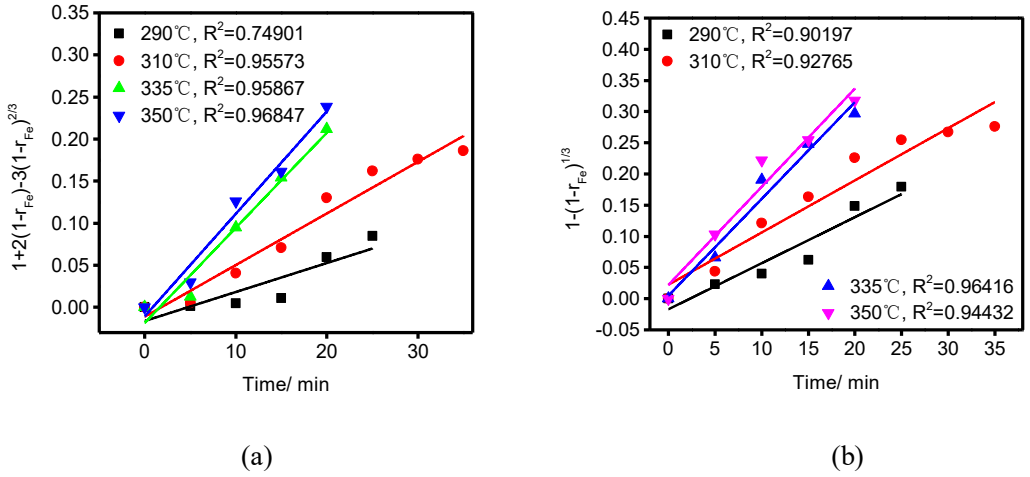

(a) (b)

Figure 12; Comparison of plots of (a) $1 + 2(1 - r_{Fe}) - 3(1 - r_{Fe})^{2/3}$ and (b) $1 - (1 - r_{Fe})^{1/3}$ vs time.

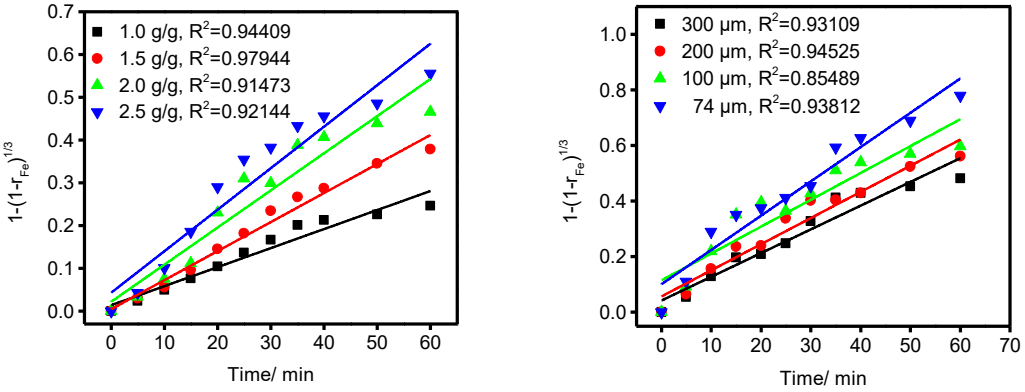

(a) (b)

Figure 13: Plots of $1 - (1 - r_{Fe})^{1/3}$ vs time for different parameters: (a) ratio of NH_4Cl to EBFS mass and (b) particle size.

Table 5: Integrated rate equations for the shrinking core model.

Rate-controlling step	Rate equation
Diffusion control through the particle layer	$1 + 2(1 - rFe) - 3(1 - rFe)^{2/3} = kr1t$
Surface chemical reaction	$1 - (1 - rFe)^{1/3} = kr2t$

rFe- iron removal degree; *t*- time (min); *kr*- apparent rate constant (min^{-1}).

This indicates that the calcination rate was controlled by chemical reaction. Fitting the experimental data presented in Figures. 6–7 with chemically-controlled model. The fitting results of the model to the experimental data is shown in Figure 13. The reaction rate constant k_r and its fitting equation are presented in Table 6.

The apparent rate constant *kr* is affected by the calcination temperature, concentration of calcination additives and EBFS particle radius. The empirical formulas can be established as per Eq. (4) [26]. Therefore, the apparent rate constant can be calculated by the relationships between *kr* and each factor.

$$k_r = \frac{kC_0M}{\rho r_0} \tag{4}$$

Where *kr* is the apparent rate constant, *k* is the reaction rate constant, C_0 is the concentration of hydrogen chloride gas, *M* is the molecular weight of solid reactant, r_0 is the initial radius of solid reactant, and ρ is the density of solid reactant (ρ = 1.8944 g/cm³).

The relationship between *kr* and calcination temperature obeys the Arrhenius equation as expressed in Reactions (2) and (3), with the results shown in Figure 14a. The apparent activation energy of iron removal is calculated to be 42.05 kJ/mol, the relationship between *kr*

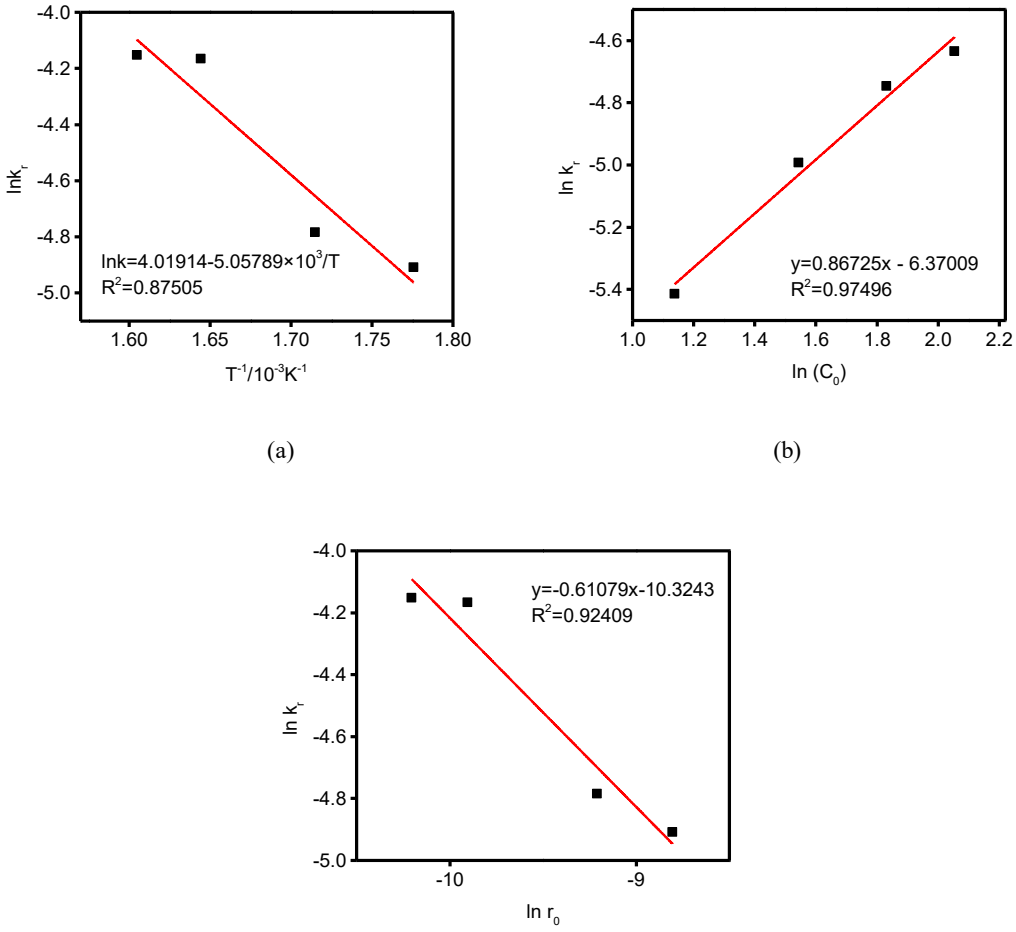

Figure 14: Relationships between ln*kr* and 1/*T*, ln(C_0), and lnr_0: (a) Arrhenius plot of the calcination process at 290, 310, 335 and 350 °C; (b) relationship between ln*k* and ln(C_0); and (c) relationship between ln*k* and lnr_0.

and *T* can be expressed as per Equation (5). It is generally believed that high values of activation energy (>40 kJ/mol) indicate chemical control, whereas values <20 kJ/mol imply diffusion-controlled processes [18-27-28], so the calcination rate was controlled by chemical reaction.

$$kr = 55.65e^{-42051/RT} \quad (5)$$

Equation (4) shows that the apparent rate constant *kr* is positively proportional to the concentration of calcination additives. The concentration of hydrogen chloride gas can be calculated by the mass ratio of NH_4Cl to EBFS. When $\frac{kM}{\rho r_0}$ is regarded as a constant, A_1, Equation. (4) can be transformed into:

$$\ln k_r = lnC_0 + lnA_1 \quad (6)$$

The plot of ln*kr* versus lnC_0 is shown in Figure 14b. The slope of the fitting line is 0.86725, so the relationship between *kr* and C_0 is:

$$kr = A_1 C_0^{0.86725} \quad (7)$$

The radius of EBFS can be calculated by its particle size. When $\frac{kC_0M}{\rho}$ is regarded as the constant A_2, Eq. (4) can be transformed into:

$$\ln k_r = \ln A_2 - \ln_{r0} \quad (8)$$

The plots of ln*kr* versus lnr_0 are presented in Figure 14c. The slope of the fitting line is 0.61079, so the relationship between *kr* and r_0 can be written as:

$$k_r = \frac{A_2}{r_0^{0.61079}} \quad (9)$$

Table 6: Parameters of $1 - (1 - r_{Fe})^{1/3}$ vs time for all experimental data.

	Apparent rate constant k	Fitting equation
Temperature (℃)		
290	0.00738	$1 - (1 - rFe)^{1/3} = 0.00738$ t
310	0.00836	$1 - (1 - rFe)^{1/3} = 0.00836$ t
335	0.01551	$1 - (1 - rFe)^{1/3} = 0.01551$ t
350	0.01573	$1 - (1 - rFe)^{1/3} = 0.01573$ t
Ratio of NH_4Cl to EBFS mass (g/g)		
1.0	0.00445	$1 - (1 - rFe)^{1/3} = 0.00445$ t
1.5	0.00679	$1 - (1 - rFe)^{1/3} = 0.00679$ t
2.0	0.00869	$1 - (1 - rFe)^{1/3} = 0.00869$ t
2.5	0.00971	$1 - (1 - rFe)^{1/3} = 0.00971$ t
Particle size (μm)		
300	0.00853	$1 - (1 - rFe)^{1/3} = 0.00853$ t
200	0.00941	$1 - (1 - rFe)^{1/3} = 0.00941$ t
100	0.00966	$1 - (1 - rFe)^{1/3} = 0.00966$ t
74	0.01233	$1 - (1 - rFe)^{1/3} = 0.01233$ t

The relationships between the three factors and *kr* are established in Eqs. (5), (7) and (9). The semi-empirical kinetic equation can be obtained by synthesizing the three relationships.

$$k_r = \frac{kC_0M}{\rho r_0} = \frac{kC_0^{0.86725}M}{\rho r_0^{0.61079}} = \frac{C_0^{0.86725}M}{\rho r_0^{0.61079}} A_3 e^{-\frac{E_a}{RT}}$$

$$= \frac{C_0^{0.86725}M}{\rho r_0^{0.61079}} A_3 e^{-\frac{42051}{RT}} = A' \frac{C_0^{0.86725}}{r_0^{0.61079}} e^{-\frac{42051}{RT}}$$

Where A_3 is a frequency factor, and $A' = \frac{MA_3}{\rho}$.

The Arrhenius equation obtained from Figure 14a is $kr = 55.65e^{-42051/RT}$, then $A' \frac{C_0^{0.86725}}{r_0^{0.61079}} = 55.65$.

Substituting C_0 = 4.68 mol/L and r_0 = 100 × 10^{-6} m gives A' = 5.26 × 10^{-2}. Therefore, the semi-empirical kinetic equation is

$$1 - (1 - r_{Fe})^{\frac{1}{3}} = 5.26 \times 10^{-2} \times \frac{C_0^{0.86725}}{r_0^{0.61079}} \times e^{-\frac{42051}{RT}} \times t$$

where r_{Fe} is the fraction of Fe removed, C_0 is the concentration of hydrogen chloride gas, r_0 is the initial radius of solid reactant, R is the molar gas constant (R = 8.314 J/mol), T is the calcination temperature (K), t is the reaction time (min).

4 Conclusions

The main minerals of EBFS are titanium carbide (TiC) and some amorphous substances. EBFS contains about 4.39% Fe_2O_3 and the distribution of the iron component is very dispersed. Besides, both Fe^{2+} and Fe^{3+} species were present in the EBFS. Removal of the iron component from EBFS uses ammonium chloride calcination. It was found that the increase of calcination temperature, mass ratio of NH_4Cl to EBFS and the decrease of slag particle size are beneficial to iron removal from EBFS. Iron is removed in the form of ferric chloride gas, the separation and recovery of ferric chloride and ammonium chloride which decomposition from reaction system can be carried out by recrystallization. The bagdasarrym model was used to describe the calcination process at temperatures below 261°C. The calculated apparent activation energy was 67.21 kJ/mol and the reaction product was ferric chloride in an amorphous solid state. The kinetic equation is $\ln[-\ln(1 - r_{Fe})] = ln12.23 \times 10^3 e^{-\frac{67210}{RT}} + lnt$. The experimental results at calcination temperature above 261 °C are matched the shrinking core model with surface chemical control, and the apparent activation energy of iron removal in the calcination reaction was estimated to be 42.05 kJ/mol. The relationships between the rate constants and the process parameters were established. The kinetic equation is $1 - (1 - r_{Fe})^{\frac{1}{3}} = 5.26 \times 10^{-2} \times \frac{C_0^{0.86725}}{r_0^{0.61079}} \times e^{-\frac{42051}{RT}} \times t$.

References

[1] Kuwahara Y., Ohmichi T., Kamegawa T., Mori K., Yamashita H., A novel conversion process for waste slag: synthesis of a hydrotalcite-like compound and zeolite from blast furnace slag and evaluation of adsorption capacities, Journal of Materials Chemistry, 2010, 20, 5052-5062.

[2] Zhou A., Lu P., Study on the Track and Recycle of Vanadium in the Titanium Extraction from Blast Furnace Slag, Iron Steel Vanadium Titanium, 2015, 36, 63-67.

[3] Zhu H., Wang P., Zhang J., Wang B., Effects of Chlorination Titanium Blast Furnace Slag on Strength and Microstructure of Mortar, Journal of Building Materials, 2011, 14, 443-446.

[4] Zhu H., Wang P., Zhang J., Wang B., Preparation of bricks by using titanium-extracted Pangang BF waste slag, New Building Materials, 2010, 37, 31-33.

[5] Liu R., Gao J., Jiang Z., Experimental Study on Manufacture Hollow Bricks from Titanium-Extracting Chlorinated Residue, Brick & Tile, 2009, 7-10.

[6] Sun H., You H., Peng T., Ding W., Zeng L., A Method of Preparing Glass-ceramics from Ti-extraction blast furnace slag, CHN Patent 2018110880519, 2018.

[7] Sun H., You H., Peng T., Ding W., Zeng L., Ma J, A Method of Preparing Glass-ceramics from heating slag in Ti-extraction blast furnace slag, CHN Patent 201811317399.0., 2018.

[8] Taxiarchou M., Panias D., Douni I., Paspaliaris I., Kontopoulos A., Removal of iron from silica sand by leaching with oxalic acid, Hydrometallurgy, 1997, 46, 215-227.
[9] National Bur. Stand. (U.S.) Monogr., 1981, 25, 73.
[10] Bahrami A., Pech-Canul M., Gutiérrez C., Soltani N., Wetting and reaction characteristics of crystalline and amorphous SiO_2 derived rice-husk ash and SiO_2/SiC substrates with Al–Si–Mg alloys, Applied Surface Science, 2015, 357, 1104-1113.
[11] Weckhuysen B.M., Wang D., Rosynek M.P., Lunsford J.H., Conversion of methane to benzene over transition metal ion ZSM-5 zeolites: I. Catalytic characterization, Journal of catalysis, 1998, 175, 338-346.
[12] Yamashita T., Hayes P., Analysis of XPS spectra of Fe^{2+} and Fe^{3+} ions in oxide materials, Applied Surface Science, 2008, 254, 2441-2449.
[13] Tan P., Active phase, catalytic activity, and induction period of Fe/zeolite material in nonoxidative aromatization of methane, Journal of Catalysis, 2016, 338, 21-29.
[14] Li H., Yang Y., Wen Y., Liu L., A mechanism study on preparation of rayon based carbon fibers with $(NH_4)_2SO_4/NH_4Cl$/ organosilicon composite catalyst system, Composites Science and Technology, 2007, 67, 2675-2682.
[15] Santos F., Brocchi E., Araújo V., Souza R., Behavior of Zn and Fe content in electric arc furnace dust as submitted to chlorination methods, Metallurgical and Materials Transactions B, 2015, 46, 1729-1741.
[16] Sui L., Zhai Y., Reaction kinetics of roasting high-titanium slag with concentrated sulfuric acid, Transactions of Nonferrous Metals Society of China, 2014, 24, 848-853.
[17] Levenspiel O., Chemical reaction engineering, Industrial & Engineering Chemistry Research, 1999, 38, 4140-4143.
[18] Sohn H.Y., Wadsworth M.E., Rate processes of extractive metallurgy, Springer Science & Business Media, 2013.
[19] Han Q., Metallurgical Process Dynamics, Metallurgical industry press, Beijing, 1983, 50-53.
[20] Hua Y., Introduction to Metallurgical Process Dynamics, Metallurgical industry press, Beijing, 2004, 306-309, 147-152.
[21] Khawam A., Flanagan D.R., Solid-state kinetic models: basics and mathematical fundamentals, The journal of physical chemistry B, 2006, 110, 17315-17328.
[22] Shi W., Wang J., Zhu G., Kinetics on chlorinating rare earth of Baotou mixed concentrate after fixed fluorine treatment, The Chinese Journal of Nonferrous Metals, 2004, 14, 1254-1258.
[23] Zhang S., Nicol M.J., Kinetics of the dissolution of ilmenite in sulfuric acid solutions under reducing conditions, Hydrometallurgy, 2010, 103, 196-204.
[24] Wang X., Srinivasakannan C., DUAN X., Peng J., Yang D., Leaching kinetics of zinc residues augmented with ultrasound, Separation and Purification Technology, 2013, 115, 66-72.
[25] Alkan M., Doğan M., Dissolution kinetics of colemanite in oxalic acid solutions, Chemical Engineering and Processing: Process Intensification, 2004, 43, 867-872.
[26] Zheng F., Chen F., Guo Y., Jiang T., Travyanov A.Y., Qiu G., Kinetics of hydrochloric acid leaching of titanium from titanium-bearing electric furnace slag, JOM, 2016, 68, 1476-1484.
[27] Habashi F., Principles of extractive metallurgy. 1. General principles, Gordon and Breach, 1969.
[28] Santos F.M., Pina P.S., Porcaro R., Oliveira V.A., Silva C.A., Leão V.A., The kinetics of zinc silicate leaching in sodium hydroxide, Hydrometallurgy, 2010, 102, 43-49.